Materials Science and Engineering A xxx (2008) xxx–xxx

Contents lists available at ScienceDirect

Materials Science and Engineering A

journal homepage: www.elsevier.com/locate/msea

A ballistic material model for cross-plied unidirectional ultra-high molecular-weight polyethylene fiber-reinforced armor-grade composites

M. Grujicic[a,*], G. Arakere[a], T. He[a], W.C. Bell[a], B.A. Cheeseman[b], C.-F. Yen[b], B. Scott[b]

[a] International Center for Automotive Research CU-ICAR, Department of Mechanical Engineering, Clemson University, 241 Engineering Innovation Building, Clemson, SC 29634-0921, United States
[b] Army Research Laboratory-Survivability Materials Branch, Aberdeen, Proving Ground, MD 21005-5069, United States

ARTICLE INFO

Article history:
Received 17 May 2008
Received in revised form 27 July 2008
Accepted 28 July 2008
Available online xxx

Keywords:
Flexible armor
Armor-grade composites
Material model
High-performance fibers
Ballistic performance

ABSTRACT

The known fiber and polymeric-matrix material properties, unit-cell microstructural characteristics and unit-cell level finite-element analyses are used to construct a new ballistic material model for 0°/90° cross-plied oriented polyethylene fiber-based armor-grade composite laminates. The model is constructed in such a way that it can be readily integrated into commercial finite-element programs like ANSYS/Autodyn [ANSYS/Autodyn version 11.0, User Documentation, Century Dynamics Inc., a subsidiary of ANSYS Inc., 2007] and ABAQUS/Explicit [ABAQUS version 6.7, User Documentation, Dessault Systems, 2007] as a user material subroutine. To validate the model, a series of transient non-linear dynamics simulations of the transverse impact of armor-grade composite laminates with two types of bullets/projectiles is carried out. The results obtained are next compared with their experimental counterparts. This comparison revealed that a relatively good agreement is obtained between the experimental and the computational analysis relative to: (a) the success of the armor panels of different areal densities in defeating the bullets at different initial bullet velocities; (b) post-mortem spatial distribution of damage within the panels; (c) the temporal evolution of a bulge at the back-face of the armor; and (d) the existence of three distinct armor-penetration stages (i.e. an initial filament shearing/cutting dominated stage, an intermediate stage characterized by pronounced filament/matrix de-bonding/decohesion and the final stage associated with the extensive bulging of the armor panel).

1. Introduction

Many light-weight ballistic-protection armor systems are currently being made of the so-called "ballistic-grade" or "armor-grade" composites (e.g. [3,4]). These composites are generally constructed using high-modulus/high-strength polymeric fibers such as aramid (e.g. Kevlar®, Twaron®, etc.) or oriented polyethylene fibers (e.g. Spectra®, Dyneema®, etc.) with an outstanding impact resistance [5–9]. The fibers, in the form of either woven fabrics or in the form of 0°/90° cross-plied collimated continuous filaments, are embedded in the resin/polymer matrix. To attain maximum utilization of the inherently high transverse-impact resistance of the fibers, the polymer-matrix content does not typically exceed 20 vol.%. As a result of the very low resin content, these composites remain flexible to relatively high laminate thicknesses. Penetration resistance of the armor-grade composites can be further increased through the use of hybrid structures in which a hard metallic or ceramic strike-plate is attached to the front of an armor-grade composite laminate.

Armor-grade composite laminates based on aramid fiber-reinforced phenolic-poly-vinyl-butyral resin and on 0°/90° cross-plied oriented polyethylene fiber-reinforced vinyl-ester resin are widely used in hard personnel-armor systems (e.g. protective helmets) for protection against fragments from exploding munitions [9–14]. These armor-grade composites are also increasingly being used for ballistic protection in light-weight armored vehicles, helicopters, patrol boats and transportable shelters (e.g. command shelters) [8]. Furthermore, hybrid armor-grade composite structures with ceramic front strike-plates have been developed for bullet-protective armor systems.

The ballistic-impact protection resistance of composite materials used in the aforementioned armor applications is typically

* Corresponding author at: Tel.: +1 864 656 5639; fax: +1 864 656 4435.
E-mail address: mica.grujicic@ces.clemson.edu (M. Grujicic).

0921-5093/$ – see front matter © 2008 Elsevier B.V. All rights reserved.
doi:10.1016/j.msea.2008.07.056

assessed in terms of two basic parameters: (a) a critical level of the projectile's velocity or the projectile's kinetic energy (generally referred to as the "ballistic limit") below which no full perforation of the armor takes place [14,15]; and (b) an extent to which material ballistic-protection resistance is compromised in the armor systems which are partially penetrated with projectile(s) or whose strike-face surface is damaged by the projectile(s).

Over the past decade, considerable efforts have been invested in carrying out various experimental investigations in order to identify and elucidate various penetration-failure mechanisms of the armor-grade fiber-reinforced composites under transverse-impact loading and to compare and contrast these mechanisms with those operating in the related resin-free fabrics and resin-rich "structural-grade" composites. The main results obtained in these investigations can be summarized as follows [16–23]:

(a) In sharp contrast to the penetration of resin-free fabrics which is dominated by the successive fracture of individual yarns along the periphery of the penetrator head and by the sideway/lateral movement of the yarns which enables them to slip off from the penetrator, the penetration of armor-grade composites is mainly governed by the failure of principal yarns (the yarns which are in direct contact with the penetrator head). This observation is attributed to the effect of resin matrix on reducing yarn mobility which prevents them from slipping off from the penetrator. In general, stiffer resin matrices (e.g. vinyl ester vs. polyurethane) constrained the yarn movement to a greater degree and force the penetrator to engage and fracture more yarns. As a result, armor-grade composites reinforced with woven-yarn fabric are generally found to possess a higher energy-absorption potential than their resin-free fabric counterparts. However, as will be discussed in more detail later, excessive confinement of the yarns/filaments in collimated unidirectional armor-grade composites may have a deleterious effect on the ballistic-protection performance of this type of armor.

(b) Since the energy absorbed by the armor-grade composite is found to scale with the number of broken yarns in its fabric constituent, fiber tensile-straining and ultimate fracture is believed to be the dominant mechanism for absorption of the projectile kinetic energy.

(c) In addition to fiber fracture, both woven fabric-reinforced and cross-plied fiber-reinforced composite laminates are generally found to include additional complex failure processes such as: (i) delamination, (ii) a plug punch-out, (iii) resin matrix cracking, and (iv) fiber pull-out. These failure modes are also typically observed in conventional structural-grade composites reinforced with glass or carbon fibers.

(d) In the case of multi-ply armor-grade composite laminates reinforced with either cross-plied collimated Spectra fibers or with woven Spectra fabrics, the following fracture modes are most often observed: (i) sequential delamination, (ii) plug punch-out induced by the through-the-thickness shear, and (iii) combined fiber shearing/cutting and fiber tensile failure. In the cross-plied laminates, fibers in the top plies are typically found to fail by shearing/cutting, primarily along the edges of the projectile. Fibers located in the back layers of the laminates, on the other hand, generally fail in tension although in thin laminates, the lateral motion of fibers and/or fiber pull-out rather than fiber tensile-straining to fracture is sometimes observed.

(e) The delamination in the cross-plied Spectra fiber-reinforced composite laminates is typically found to resemble the "generator strip" phenomenon [22] seen in conventional composites reinforced with glass fiber-reinforced epoxy resin. That is, under transverse impact, the projectile pushes a strip of the first lamina toward the rear of the laminate which induces shear cracks in the resin matrix parallel to the fibers and applies a transverse load to the second lamina. This, in turn, causes separation between the first two laminates, i.e. delamination. After the successive delamination had taken place through the entire thickness of the laminate via the same mechanism and penetration of the laminate has occurred, narrow strips of damage zone remain visible under the transmitted light and the strips are found to tend to follow the respective fiber orientation in the panel. These strips typically contain numerous matrix/fiber interface cracks. In addition, a circular delamination zone is generally seen around the perforation hole.

(f) In contrast to the case of cross-plied fiber-reinforced composite laminates, fabric-reinforced laminates exhibited much less lateral movements of reinforcing fibers during the penetration of the projectile [3,4]. Even in thin panels, fibers apparently failed due to shearing/cutting in the laminae near the strike-face and in tension at the rear of the completely penetrated laminates. The presence of a narrow strip of the first lamina pushed forward by the penetrator is generally not observed. Instead, the delamination zones are observed preferentially along the two reinforcement directions of woven fabric. However, these damage zones are closely integrated with the circular delamination zone around the perforation hole. The occurrence of less anisotropic pattern of delamination was linked with the presence of resin-rich pockets between the reinforcing layers and with a greater constraint to matrix crack propagation parallel to the fibers/yarns.

(g) Up to the thickness of ~3 mm, the dependence of the kinetic energy for full perforation of armor-grade composites on the laminate thickness is similar to that observed in ductile monolithic materials such as poly-carbonate or aluminum but displays some non-linearity which is attributed to their unique mode of tensile failure for which the critical level of kinetic energy for full perforation is lowered by the fiber/yarn mobility.

The first use of fiber-based composites (primarily nylon (polyamide) fabric and E-glass fiber/ethyl cellulose composites) in body-armor systems in place of the traditionally used metallic solutions can be traced back to the Korean war [24]. Although, primarily due to their low cost, nylon and E-glass fibers are still being used today, high-performance polymeric fibers are now the standard in most fiber-reinforced body-armor applications. The high-performance polymeric fibers used today are characterized by substantially improved strength, stiffness and energy-absorbing capacity. Among these high-performance fibers the most notable are: (a) poly-aramids (e.g. Kevlar®, Twaron®, Technora®); (b) highly oriented ultra-high molecular-weight polyethylene, UHMWPE (e.g. Spectra®, Dyneema®); (c) poly-benzobis-oxazole, PBO (e.g. Zylon®), and (d) poly-pyridobisimi-dazole, PIPD (e.g. M5®). When tested in tension, all these materials differ significantly from the nylon fibers, having very high absolute stiffness, extremely high specific strength, and quite low (<4%) strains-to-failure. These fibers essentially behave, in tension, as rate-independent linear elastic materials. When tested in transverse compression, however, these fibers are similar to nylon and can undergo large plastic deformation without a significant loss in their tensile load-carrying capacity. This behavior is quite different from that found in carbon or glass fibers, which tend to shatter under transverse compression loading conditions.

The ballistic performance of high-performance polymeric fibers is, in general, quantified with respect to their ability to: (a) absorb the projectile's kinetic energy locally; and (b) spread out the absorbed energy fast before local conditions for the failure are met. In simple terms, the ability of high-performance fibers to absorb

Please cite this article in press as: M. Grujicic, et al., Mater. Sci. Eng. A (2008), doi:10.1016/j.msea.2008.07.056

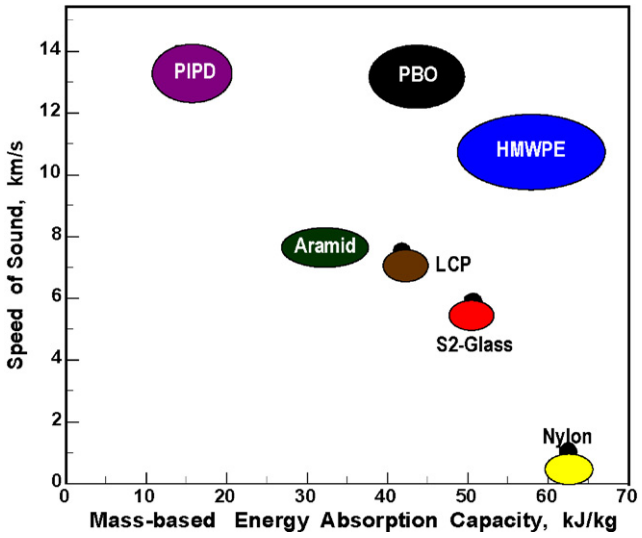

Fig. 1. Sound speed vs. mass-based energy-absorption capacity for a number of high-performance fibers.

energy per their unit mass, E_{sp}, is related to the fiber tenacity/failure strength, σ_{fail}, the fiber strain-to-failure, ε_{fail}, and the fiber density, ρ, as:

$$E_{sp} = \frac{0.5\sigma_{fail}\varepsilon_{fail}}{\rho} \quad (1)$$

The ability of fibers to spread out energy is governed by their speed of sound, v_{sound}, which is defined in terms of their axial modulus of elasticity, E, and their density as:

$$v_{sound} = \left(\frac{E}{\rho}\right)^{(1/2)} \quad (2)$$

A summary of the key properties of the most-commonly used high-performance fibers is provided in Table 1. In Fig. 1, the two ballistic performance parameters are displayed for the same set of high-performance fibers.

While the results displayed in Fig. 1 clearly reveal a high ballistic potential of the high-performance fibers in general (and specifically of the highly oriented UHMWPE fibers, the type of fiber-reinforcements considered in the present work), full utilization of this potential in armor-grade composites turned out to be a formidable challenge because a number of additional factors (e.g. fabric/ply structure/architecture, ply areal density, fiber-to-fiber/yarn-to-yarn and fiber/yarn-to-projectile friction, type of polymeric matrix, composite processing and fabrication conditions, shape, mass and mechanical properties of the projectile to be defeated, etc.) become important. To overcome these challenges, the development of flexible-armor systems has started to rely increasingly more on the use of transient non-linear dynamics computational analyses of the ballistic response of armor when impacted with high-speed projectiles. For these analyses to yield reliable predictions and for them to be used as complements to the accompanying experimental investigations, high-fidelity physically based material models for the armor-grade composite materials must be available.

A review of the public-domain literature carried out as part of the present work revealed the existence of several material models for armor-grade composite materials [25–30]. While such models have provided an important insight into the roles of a number of factors mentioned above, they suffer from three major shortcomings: (a) they are more phenomenological, i.e. less physically based in their character; (b) they require the knowledge of a relatively large number of parameters; and (c) they are not very efficient computationally. These shortcomings seriously jeopardize the utility of the computational engineering analyses in the design and optimization of flexible-armor systems for different projectile types and sizes. In addition to the models mentioned above, purely phenomenological models (e.g. [31]) also exist in the literature. Such models are the result of extensive experimental efforts and typically have, within the same family of armor-grade composite materials, a high practical utility. However, they provide no insight into the complicated physics of projectile/armor interactions and cannot be used across the boundaries of different armor-type composite families.

To overcome the aforementioned limitations of the two groups of material models, a new physically based computationally efficient material model for UHMWPE filament (e.g. Spectra®, Dyneema®, etc.)-based armor-grade composites is developed, parameterized and validated in the present work. Since it was found that for the UHMWPE fiber-based armor-grade composites, a substantially higher ballistic performance is obtained when such fibers are used as 0°/90° cross-plied unidirectional layers of filaments rather than woven fabrics, only the former composite-laminate architecture will be addressed in the present work. In passing, it should be mentioned that it is believed that the deflection of stress waves at the yarn/yarn or fiber/fiber cross-ever points in woven fabric is the main reason for their inferior ballistic performance.

The organization of the paper is as follows: details regarding the computational procedures employed to develop a new unit-cell continuum-damage-based material model for a prototypical 0°/90° cross-plied unidirectional UHMWPE filament-based armor-grade composite and the implementation of this model into a material user subroutine suitable for use in commercial finite-element programs are presented in Section 2. The formulation of a simple projectile-armor impact problem used to validate the new material model is described in Section 3. Main results obtained in the current work are presented and discussed in Section 4. The main summary points and conclusions resulting from the present work are listed in Section 5.

2. Development of the material model

In this section and its subsections, a detailed account is given of the procedure used to develop a new unit-cell continuum-damage-based material model for a prototypical single-lamina 0°/90° cross-plied unidirectional UHMWPE filament-based armor-grade composite. Also details regarding the implementation of the model into a material user subroutine suitable for use in commercial finite-element packages are presented. The basic idea behind the unit-cell-based approach is that the mechanical response of the armor unit-cell (consisting of high-stiffness/high-strength polymeric filament segments and a compliant polymeric matrix) can be smeared out (homogenized) into an equivalent response of a (anisotropic) continuum material. A simple schematic of the unit-cell which is used to represent 0°/90° cross-plied unidirectional UHMWPE filament-based armor-grade composites allotted to a single filament crossover is depicted in Fig. 2(a). Its continuum-level material point counterpart is represented in Fig. 2(b). Within the continuum-material framework, filaments are not represented explicitly but rather by two material directions whose orientations are denoted in terms of material vectors, $\mathbf{g}_1$ and $\mathbf{g}_2$. (Please note that vectors are denoted using a bold lower-case font, tensors using a bold upper-case font while scalars using a non-bold font.) The "unit-cell" term is used to denote the basic structural block so that

Table 1
Typical mechanical properties of high-performance fibers

Fiber type	Failure strength (GPa)	Failure strain	Axial modulus (GPa)	Density (kg/m^3)
Aramid	2.8–3.2	0.015–0.045	60–115	1390–1440
HMWPE	2.8–4.0	0.029–0.038	90–140	970–980
LCP	2.7–2.9	0.033–0.035	64–66	1400–1420
PBO	5.4–5.6	0.024–0.026	270–290	1540–1560
PIPD	3.9–4.1	0.011–0.013	320–340	1690–1710
Nylon	0.06–0.08	1.5–2.5	1.0–1.5	1070–1170
S-glass	4.64–4.66	0.053–0.055	82–92	2470–2490

a piece of the armor-grade composite material can be considered as a result of the repetition of this block in three orthogonal directions.

Coupling between the continuum-material formulation and the unit-cell geometry and mechanical response is done in the following way: (a) the deformation state of a continuum-material point (as quantified by the corresponding deformation gradient) is used to update the unit-cell geometry; (b) the updated unit-cell geometry and the state of the continuum material at the end of the previous time increment are used to update the extent of structural damage in the unit-cell; and (c) the updated material state obtained in point (b) is then used to compute the stress state at the end of the current time increment.

It must be noted that in order for the aforementioned approach to be valid (i.e. in order for homogenization of the armor-grade composite unit-cell response to be justified), the characteristic lengths in the numerical analysis in which the model is used (e.g. the projectile and the armor dimensions in a projectile/armor impact problem analyzed in the present work and the associated stress/strain gradient ranges) must be large in comparison to the unit-cell edge lengths. In most practical situations, this appears to be the case since the unit-cell edge length is in the range between 10 and 30 μm.

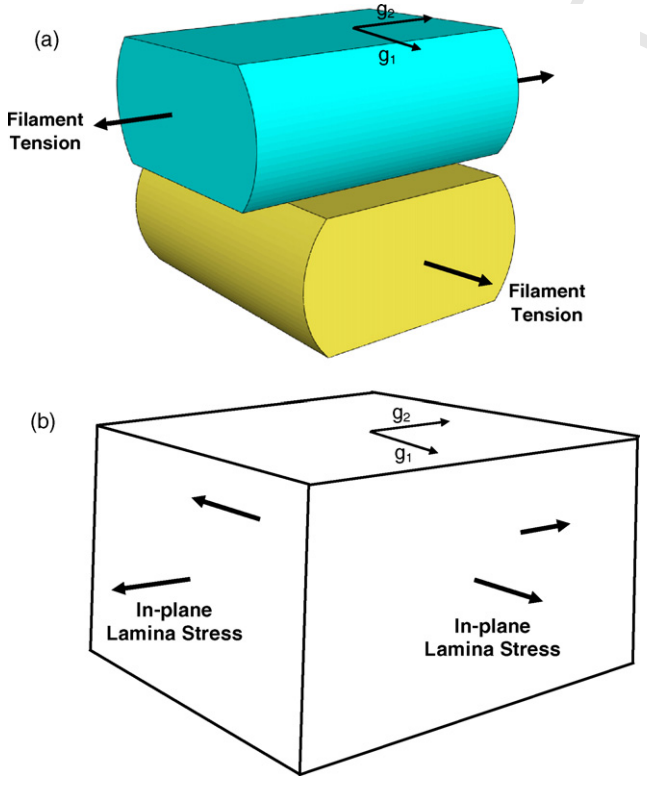

Fig. 2. The relationship between a unit-cell and the corresponding material point in an anisotropic continuum.

2.1. Unit-cell level finite-element analyses

The salient feature of the proposed computational approach is that the mechanical response of a continuum-level material point (corresponding to a unit-cell in the armor-grade composite) and the accompanying changes in constituent materials (primarily those associated with the filament/matrix interfacial de-bonding) can be inferred by carrying out a series of finite-element analyses pertaining to relatively simple mechanical tests of the unit-cell. In these analyses, a detailed representation of the unit-cell microstructure is considered. In this section, details are presented regarding the geometrical models used in the construction of the unit-cell, material models assigned to the filament segments, matrix and the filament/matrix interfacial bonding, and the finite-element analyses used to determine the mechanical response and the material evolution under different loading conditions.

An example of the finite-element meshes used in the unit-cell computational analyses is displayed in Fig. 3(a) and (b). 20,847 first-order tetrahedron elements, C3D4, are used to discretize each of the two filament segments, Fig. 3(a), while 21,606 elements of the same type are used to discretize the matrix, Fig. 3(b). Bonding between the matrix and the filaments is represented using 7056 "cohesive" elements, COH3D6.

The polymeric filaments (assumed to be based on the UHMWPE) are modeled as orthotropic (more precisely as planar isotropic) linear elastic materials (up to the point of failure under axial tension or transverse shear) with the unique material direction being aligned with the filament axis. A summary of the elastic and failure properties of the filament material is provided in Table 2. The polymeric matrix (assumed to be based on styrene–isoprene–styrene tri-block copolymer [32]) is modeled, due to attendant high-deformation rate conditions, as a linear isotropic material with a Young's modulus of 3 GPa and a Poisson's ratio of 0.4. Bonding between the filaments and the matrix is modeled using traction vs. interfacial-displacement discontinuity relations (one for the normal and one for the tangential displacements), these two relations are characterized by a linear traction vs. displacement/discontinuity relation unto the point of damage initiation and with a linear "down-hill" post-damage relationship. Consequently the two modes "normal and shear" of interfacial-bonding damage are each characterized by three parameters: (a) critical normal

Table 2
The orthotropic linear elastic material data for UHMWPE filaments [31]

E_{11} (GPa)	118.0
E_{22} (GPa)	6.0
E_{33} (GPa)	6.0
G_{12} (GPa)	6.0
G_{13} (GPa)	6.0
G_{23} (GPa)	6.0
ν_{12}	0.3
ν_{13}	0.3
ν_{23}	0.4

Axial failure strain = 0.05; transverse shear strength = 350 MPa.

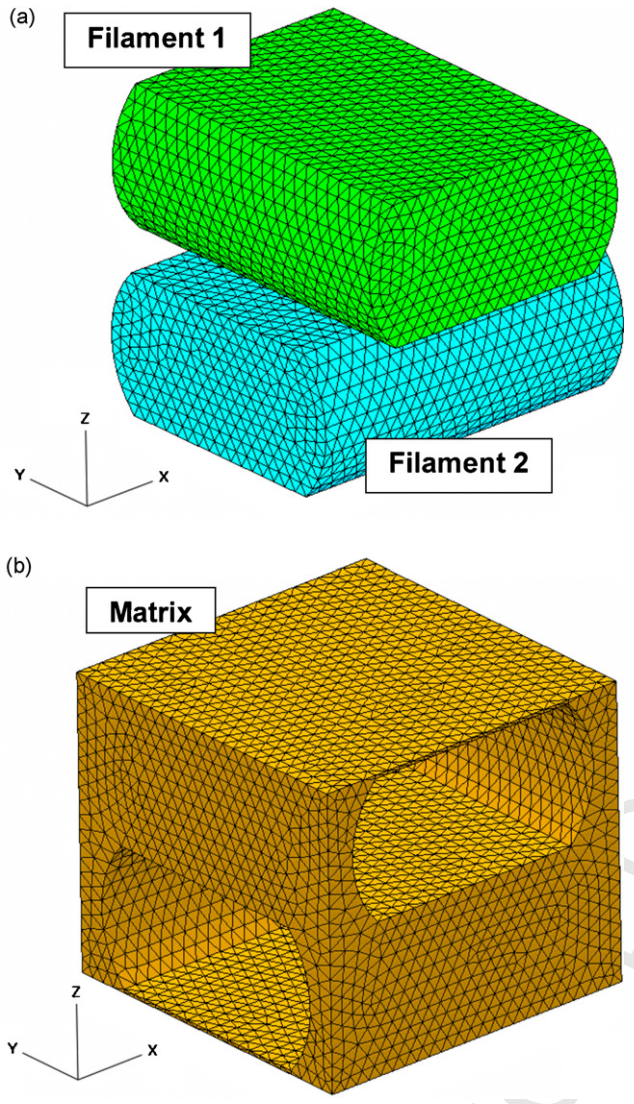

Fig. 3. Typical finite-element meshes used in the unit-cell computational analyses to discretize: (a) the two filaments and (b) the matrix.

or shear interfacial-displacement discontinuities at which damage initiation begins; (b) the corresponding normal or shear interfacial strengths; and (c) normal or shear interfacial-displacement discontinuities at which complete filament/matrix decohesion takes place. A summary of the interfacial cohesion parameters used in the present work is given in Table 3. These parameters were determined in a separate molecular-statics-based investigation of atomic-level mechanical properties of the composite materials consisting of the unidirectional UHMWPE filaments and an amorphous polymeric matrix. The results of this investigation will be reported elsewhere and the procedure used closely follows that presented in our recent work [36] in which atomic-level properties of composite materials consisting of multi-walled carbon nanotube reinforcements and a poly-vinyl-ester–epoxy matrix were investigated.

Table 3
Normal and shear filament/matrix de-bonding parameters used in the present work

Normal de-bonding	
Initiation displacement discontinuity (μm)	0.5
Bond strength (MPa)	18.0
Complete de-bonding displacement discontinuity (μm)	1.1
Shear de-bonding	
Initiation displacement discontinuity (μm)	0.9
Bond strength (MPa)	23.0
Complete de-bonding displacement discontinuity (μm)	2.1

Interactions between the filaments and the matrix after decohesion are accounted for through a "hard" pressure vs. over closure algorithm within which the interacting bodies must be in contact before they can interact and the pressure levels that can be transmitted through the contact interactions are unbounded. Relative sliding of the contacting bodies is opposed by a frictional force based on a constant friction coefficient.

The following simple mechanical tests were carried out using the unit-cell-based finite-element approach described above: (a) uniaxial tension along the axis of one of the filaments (i.e. along the direction 1 or 2); (b) uniaxial tension in a direction normal to the single-lamina surface (direction 3); (c) in-plane 1 and 2 shear; and the transverse shear. For each of these tests, a series of loading–unloading–reloading cycles was applied in order to detect the onset of interfacial de-bonding and the resulting degradation in the corresponding continuum-material stiffness parameters. To determine how one mode of loading may affect all the unit-cell stiffness parameters, loading is done in one mode while subsequent reloading is done in all the modes (one at a time).

The results obtained suggests that interfacial de-bonding is mainly caused by the through-the-thickness tension (in direction 3) and by the in-plane shear (1 and 2 shear) and that E_{33}, G_{12}, G_{23} and G_{31} are mostly degraded by interfacial de-bonding. In addition, these four stiffness parameters are found to degrade essentially linearly with the extent of interfacial-bonding damage, D. In accordance with these observations, the damage initiation criterion was defined as follows:

$$\left(\frac{\varepsilon_{33}}{\varepsilon_{33,\text{init}}}\right)^2 + \left(\frac{\gamma_{12}}{\gamma_{12,\text{init}}}\right)^2 = 1 \tag{3}$$

where $\varepsilon_{33,\text{init}}$ and $\gamma_{12,\text{init}}$ are pure normal and shear strains at which damage initiation is first observed. In a $\varepsilon_{33}/\varepsilon_{33,\text{init}}$ vs. $\gamma_{12}/\gamma_{12,\text{init}}$ plot, Eq. (3) defines a unit (failure-initiation) circle. Within the same plane, the condition at which complete damage-induced degradation takes place is defined by an ellipse in the form:

$$\left(\frac{\varepsilon_{33}}{\varepsilon_{33,\text{fail}}}\right)^2 + \left(\frac{\gamma_{12}}{\gamma_{12,\text{fail}}}\right)^2 = 1 \tag{4}$$

where $\varepsilon_{33,\text{fail}}$ and $\gamma_{12,\text{fail}}$ are pure normal and shear strains at which complete degradation ($D = 1$) takes place.

When the (ε_{33}, γ_{12}) strain state of a material point (e.g. point B in Fig. 4) lies between the damage initiation circle and the failure ellipse, the corresponding extent of material damage is defined as the ratio of line segments AB and AC indicated in Fig. 4. The four continuum-level damage parameters $\varepsilon_{33,\text{init}}$, $\varepsilon_{33,\text{fail}}$, $\gamma_{12,\text{init}}$ and $\gamma_{12,\text{fail}}$ are determined using the unit-cell finite-element analyses described in this section. The values of these four parameters are: 0.01, 0.04, 0.01 and 0.04, respectively.

2.2. Determination of the current unit-cell geometry and architecture

As discussed earlier, a critical step in the development of the present continuum-damage material model is establishment of the relationship between the continuum-level material point deformation state and the unit-cell geometry. This topic is covered in the present section.

In general six independent geometrical parameters are needed to fully describe the current geometry of the unit-cell. These parameters include: (a) the three unit-cell edge lengths, $\mathbf{a}_i$ ($i = 1–3$); (b) the in-plane shear inter-filament included angle, θ; and (c) the two out-

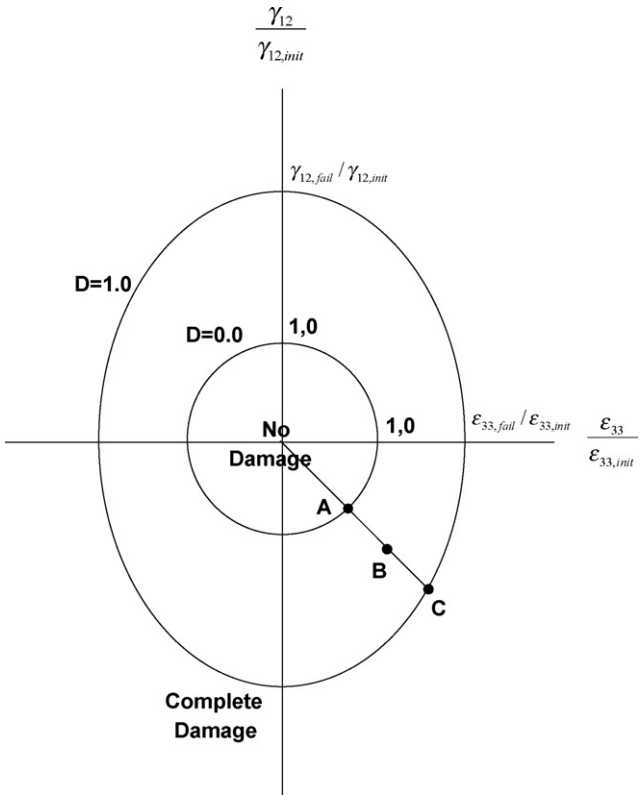

Fig. 4. A schematic of the computational procedure used to determine the onset and track the progress of material damage (interfacial de-bonding) within the unit-cell.

of-plane shear angles, ϕ and ψ. In this section it is shown how these parameters are related to the continuum-level deformation state of the material point corresponding to the unit-cell in question.

At the continuum level, the state of deformation at a given material point is described by the deformation gradient, **F**, whose components in a Cartesian coordinate system are defined as:

$$\mathbf{F}_{jk}(t) = \frac{\mathrm{d}x_j(t)}{\mathrm{d}X_k} \tag{5}$$

where $x_j(t)$ is the jth component of a material point at time t, and X_k the kth component of the same point in the initial/un-deformed configuration.

At the continuum level, the 0° and 90° filaments can be described using vectors $\mathbf{a}_i$ (i = 1 and 2) aligned with the axis of these filaments and the length of these vectors can be set equal to the corresponding current in-plane unit-cell edge lengths, $\mathbf{a}_i$ (i = 1 and 2). These vectors and the vector $\mathbf{a}_3$ which is aligned with the out-of-plane unit-cell edge can be related to their initial counterparts, $\mathbf{a}_{i,0}$ (i = 1–3) as:

$$\mathbf{a}_i = \mathbf{F}\mathbf{a}_{i,0} \quad (i = 1\text{–}3) \tag{6}$$

The length of each $\mathbf{a}_i$ (i = 1–3) can be defined as:

$$\mathbf{a}_i = \sqrt{\mathbf{a}_i \cdot \mathbf{a}_i} = \sqrt{(\mathbf{F}\mathbf{a}_{i,0}) \cdot (\mathbf{F}\mathbf{a}_{i,0})} = \sqrt{\mathbf{a}_{i,0}(\mathbf{F}^{\mathrm{T}}\mathbf{F})\mathbf{a}_{i,0}} \tag{7}$$

where the inter-filament included angle θ can be computed from:

$$\mathbf{a}_1 \cdot \mathbf{a}_2 = (\mathbf{F}\mathbf{a}_{1,0}) \cdot (\mathbf{F}\mathbf{a}_{2,0}) = \mathbf{a}_1\mathbf{a}_2 \cos\theta \tag{8}$$

An equation analogous to Eq. (8) can be used to define the out-of-plane shear angles ϕ and ψ. Eqs. (5)–(8) thus show that the current geometry of the unit-cell can be determined using the original unit-cell edge lengths and the current value of the deformation gradient.

Once the current unit-cell parameters are defined, standard relations are invoked to compute the corresponding normal and shear strains. Next, through-the-thickness normal strain ε_{33} and the in-plane shear strain γ_{12} and the procedure outlined in the previous section are used to update the extent of material damage and the affected stiffness moduli. It should be noted that material damage is irreversible, i.e. D cannot decrease during the deformation history of a material point.

2.3. Determination of the material point stress state

Once the extent of material damage is updated then E_{33}, G_{12}, G_{23} and G_{31} are degraded by multiplying their initial values by a factor $(1.0cD)$, where $0.0 \leq c \leq 1.0$ is an elastic-modulus dependent parameter. Since the continuum material is modeled as a linear elastic orthotropic material with degradable stiffness moduli, the standard relationships are used to compute the stress components from the updated strain components and the updated material stiffness matrix.

Once the stresses are updated, the occurrence of filament failure is investigated. Filaments are allowed to fail in one of the two following modes: (a) in tension, when the tensile-strain/tensile-stress reaches a critical value or (b) due to transverse shear, when the corresponding transverse shear stress reaches a critical value. When either of these two filament failure modes takes place, the corresponding in-plane normal stress(es) and the corresponding transverse shear stress are set to a small residual value associated with the remaining matrix ligaments. Once the stresses are updated to include the effect of filament failure they are ready to be returned to the finite-element solver for the computation of the global equilibrium.

The present material model is, thus, constructed in such a way so that it can account for the competition between the following two processes: (a) transverse shear loading which is promoted by good filament/matrix bonding and higher matrix stiffness. If sufficiently high transverse shear stresses are developed they can cause shear/type failure of the filament(s). In this case, the energy absorbed by the filaments is relatively small and, consequently, ballistic/protection performance of the armor-grade composite laminate is inferior; and (b) stretching of the filaments till the point of failure. This process is promoted by filament/matrix de-bonding which enables the filaments to deform independently of the matrix. In this case, the energy absorbed by the filaments is maximum and the ballistic/protection of the armor is greatly enhanced. It should be noted that some critical level of filament-matrix bonding is needed to ensure that the filaments are not simply pushed laterally by advancing projectile which can lead to the defeat of the armor by the projectile via the so-called "wedge through effect" [35].

2.4. Material model implementation in a user material subroutine

The unit-cell-based material model described in the previous section is next implemented in the material user subroutine, VUMAT, of the commercial finite-element program ABAQUS/Explicit [2]. This subroutine is compiled and linked with the finite-element solver and enables ABAQUS/Explicit to obtain the needed information regarding the state of the material and the material mechanical response during each time step, for each integration point of each element. In the present work, first-order six-node general-purpose reduced-integration solid elements (ABAQUS/Explicit designation C3D6R) are used.

The essential features of the coupling between the ABAQUS/Explicit finite-element solver and the VUMAT material user subroutine at each time increment at each integration

Table 4
Experimental [33] and the corresponding computational (present work) results pertaining to the success of armor-grade composite test panel to stop a M855 bullet at different initial bullet velocities

Test-panel thickness (mm)	Areal density (kg/m^2)	Bullet velocity (m/s)			
		600	700	800	900
4.2	4	–	–	–	G/G
11	10.5	G/G	G/G	G/G	G/G
15	13.7	–	O/O	O/O	G/G
22	21	U/U	U/U	U/U	U/U
32	31	U/U	U/U	U/U	U/U

Nomenclature: U, undermatched; O, overmatched; G, grossly overmatched; and experiment/computation.

point of each element can be summarized as follows:

(a) The corresponding previous time-increment stresses and material state variables as well as the current time-step deformation gradient are provided by the ABAQUS/Explicit finite-element solver to the material subroutine. In the present work, the strain components, two variables pertaining to the not-failed/failed status of the filaments and one variable pertaining to the deletion status of the finite element are used as the state variables.
(b) Using the information provided in (a), and the unit-cell-based material model presented in the previous section, the material stress state as well as values of the material state variable(s) at the end of the time increment are determined within the VUMAT and returned to the ABAQUS/Explicit finite-element solver. In addition, the changes in the total internal and the inelastic energies (where appropriate) are computed and returned to the solver.

3. Validation of the material model

As stated earlier, the main objective of the present work was to develop a microstructure-dependent physically based material model for the armor-grade composites based on 0°/90° cross-plied unidirectional UHMWPE filaments and a low-content (<20 mass%) polymeric matrix. In this section, a simple projectile/armor impact problem is described. The problem is used to carry out preliminary testing and validation of the proposed unit-cell continuum-damage-based material model.

Two types of full-metal jacketed bullets both of the 5.56-mm caliber were considered. The first type of bullet (M855) has a hardened steel tip attached to the lead core and a 0.5-mm thick copper jacket. The weight of this bullet is ~4.0 g and due to the presence of the hardened steel tip the bullet behaves as an armor-piercing (AP) projectile. The second bullet type (M193) does not contain the a hardened steel tip but its otherwise geometrically quite similar to the M855 bullet. The weight of the M193 bullet is ~3.5 g.

Since the computational results for the projectile/armor impact obtained in the present work were compared with their experimental counterparts obtained in the work of Iremonger [33], five armor panels with a thickness of 4.2, 11, 15, 22 and 32 mm were investigated in the present work. The corresponding armor areal densities can be found in Table 4. In each case the armor panel had a circular/disk shape with a radius of 90 mm.

An example of the initial configuration of the projectile/armor finite-element system analyzed here is shown in Fig. 5. Due to the inherent symmetry of the problem, only one quarter of the model is analyzed and the appropriate symmetry boundary conditions are applied along the planes of symmetry. Typically (one quarter of) the projectile is discretized in terms of 1955 first-order tetrahedron elements C3D4, while (one quarter of) the armor panel is discretized using 382 first-order six-node brick elements, C3D6, per 1.1-mm thick lamina. To reduce the computational burden, the size of the C3D6 elements is chosen to match that of the C3D4 elements only in the region of the armor panel impacted and greatly affected by the bullet. A courser mesh was used in the section of the armor less affected by the bullet impact.

The three metallic materials (steel, lead and copper) present in the two types of bullets are modeled using (a linear equation of state, the Johnson–Cook strength model, the Johnson–Cook failure model and an erosion algorithm based on the maximum allowable instantaneous geometrical strain). Considering the fact that these material models were reviewed in our recent work [34], they will not be discussed any further here. The armor panel was assigned the material model developed in the present work.

To define the initial-conditions, zero initial velocities were assigned to all the nodes of the armor panel while a constant velocity in the negative Z direction was assigned to all the nodes of the bullet. Four initial bullet velocities were considered: 600, 700, 800 and 900 m/s. To mimic the effect of clamping along the armor edges, fixed boundary conditions are applied to all the peripheral nodes of the armor panel.

The same hard interaction algorithm as that used in Section 2.1 was also employed to model interactions between the bullet and the armor. To account for the sliding-friction resistance between the bullet and the armor, a simple Coulomb friction model was used.

Computational analyses were run on a machine with two 2.33 GHz Quad-core Intel Xeon processors with 16 GB of RAM. A typical run involving the 11-mm thick armor panel took ~12 min while in the case of a 32-mm thick panel the wall-clock computational time was ~45 min.

4. Results and discussion

As discussed earlier, the unit-cell continuum-damage material model for 0°/90° cross-ply UHMWPE filament-based armor-grade composites is validated by comparing the computational results obtained in a series of transient non-linear dynamics finite-element analyses discussed in Section 3 with their experimental counterparts obtained in the work of Iremonger [33]. Iremonger [33] investigated five armor panels with a thickness from 4.2 to 32 mm, used two types of bullets (M855 and M193) and four initial velocities. Thus the full-factorial test matrix involves $5 \times 2 \times 4 = 40$ experiments. Not all 40 experiments were conducted in the work of Iremonger [33] and only selected results were reported for the experiments that were carried out. Three types of results were reported: (a) the success of armor in stopping the bullet. Iremonger [33] used the following nomenclature: under matched (to denote the cases when the armor was successful in stopping the bullet), overmatched (to denote the cases when the armor was fully penetrated by the bullet but was able to absorb a substantial amount of the bullets kinetic energy), and grossly overmatched (to denote the cases when the bullet was able to fully penetrate the armor by punching out a circular-disk shaped plug of the armor material without a significant loss in the bullets kinetic energy; (b) post-mortem micrographs of the vertical cut sections of the armor panel passing through the axis of the penetration hole and; (c) temporal-evolution plots for the armor back-face bulge height and the bulge diameter. In the remainder of this section, a comparison is made between the computational and the experimental results for each of these three types of results.

4.1. Outcome of the bullet impact onto the armor test panel

The success of different armor panels in stopping the M855 bullet at different bullet velocities as determined experimentally by

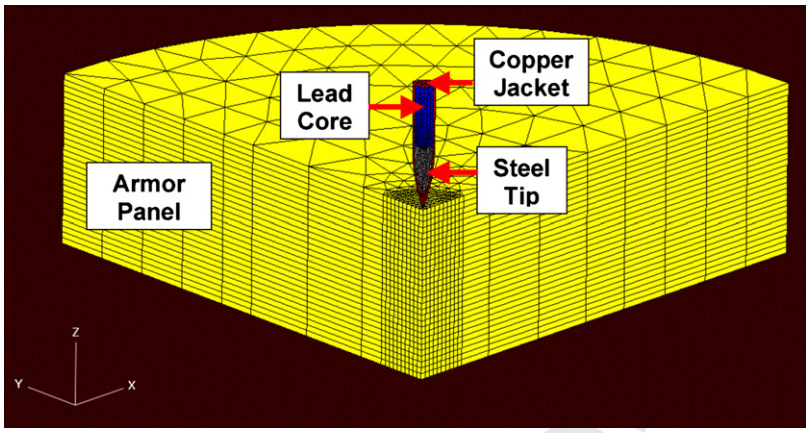

Fig. 5. Typical final element meshes used in the transient non-linear finite-element analyses of the impact of a full-jacketed metal bullet impact onto an armor-grade composite test panel. Due to inherit symmetry of the problem only one-quarter of the model is analyzed.

Iremonger [33] and computationally in the present work as displayed in Table 4. It is seen that the overall agreement between the two sets of results is quite reasonable suggesting that the proposed unit-cell continuum-damage-based material model for cross-plied UHMWPE filament-based armor-grade composites is capable of capturing the essential features of the mechanical behavior of this material under ballistic loading conditions. It is unfortunate that in Ref. [33], the results analogous to those displayed in Table 4 were not reported for the non-armor-piercing bullet M193. Hence a similar experiment/computation comparison cannot be made for this type of bullet.

4.2. Type, extent and spatial distribution of damage

In Ref. [33], three micrographs of the vertical cut sections of the armor panel (each passing through the axis of the penetration hole) were provided. Due to copyright restrictions, only schematics of these micrographs are included in the present work. The three micrographs correspond to the following armor/bullet/test conditions: (a) 11-mm thick test panel/M855/600 m/s, Fig. 6(a); (b) 22-mm thick test panel/M855/800 m/s, Fig. 7(a); (c) 22-mm thick test panel/M193/800 m/s, Fig. 8(a). The corresponding computational counterparts revealing the spatial distribution of damage in the armor panel obtained in the present work are displayed in Figs. 6(b), 7(b) and 8(b), respectively.

A comparison of the results displayed in Figs. 6(a), 7(a) and 8(a) with the ones displayed in Figs. 6(b), 7(b) and 8(b), respectively, reveals that the overall agreement between the two sets of results is reasonable. More specifically:

(a) In the case of 11-mm thick armor panel impacted by an M855 projectile at an initial velocity of 600 m/s, both the experiment, Fig. 6(a), and the numerical results, Fig. 6(b), show a "punch through" mode of penetration which is dominated by transverse shearing/cutting of the filaments and associated with relatively low absorption of the projectiles kinetic energy. In addition, the size of penetration hole and its changes through the armor-panel thickness are reasonably well reproduced by the present material model, Fig. 6(a) and (b).

(b) In the case of a 22-mm thick armor panel impacted by an M855 projectile at an initial velocity of 800 m/s, both the experiment, and the numerical results show only a partial

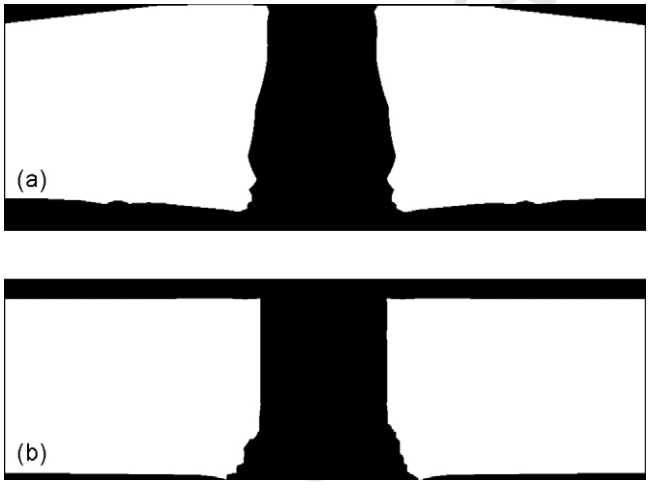

Fig. 6. A comparison between (a schematic of) the experimental results obtained in Ref. [33] (a), and their computational counterparts obtained in the present work (b), pertaining to the spatial distribution of damage in case of a M855 bullet initially propelled at a velocity of 600 m/s impacting an 11-mm thick test panel.

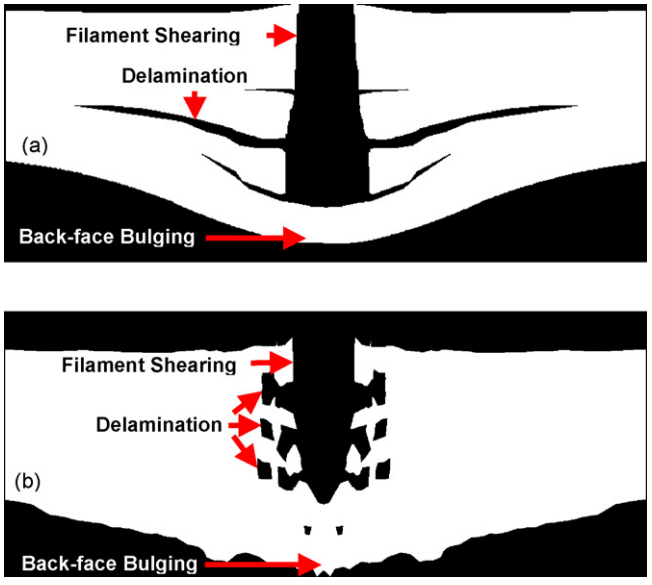

Fig. 7. A comparison between (a schematic of) the experimental results obtained in Ref. [33] (a), and their computational counterparts obtained in the present work (b), pertaining to the spatial distribution of damage in case of a M855 bullet initially propelled at a velocity of 800 m/s impacting a 22-mm thick test panel.

Please cite this article in press as: M. Grujicic, et al., Mater. Sci. Eng. A (2008), doi:10.1016/j.msea.2008.07.056

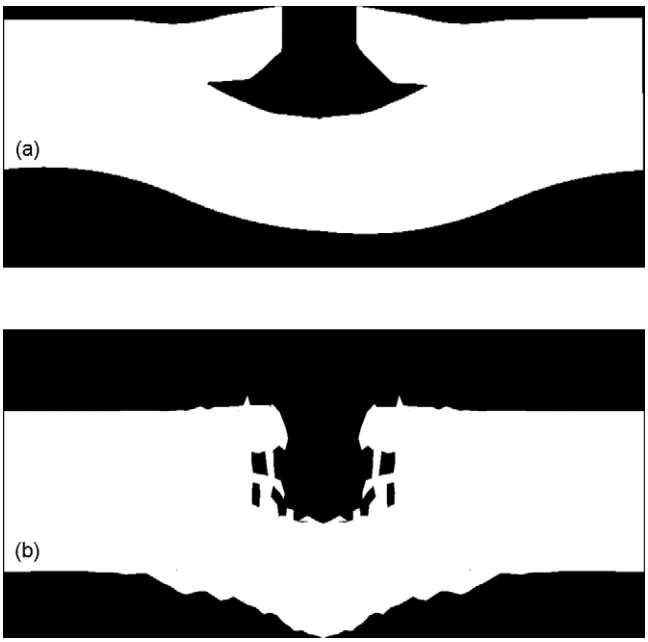

Fig. 8. A comparison between (a schematic of) the experimental results obtained in Ref. [33] (a), and their computational counterparts obtained in the present work (b), pertaining to the spatial distribution of damage in case of a M193 bullet initially propelled at a velocity of 800 m/s impacting a 22-mm thick test panel.

penetration of the armor, Fig. 7(a) and (b). In the same figures it is seen that the depth of the penetration hole is some what under predicted by the computational analyses. On the other hand, both the experiment and the computational analysis predict that initial penetration of the armor panel is first dominated by filament shearing/cutting and subsequently by filament/matrix de-bonding/delamination. It should be noted that the present material model is based on the use of a homogenization technique which yields an equivalent single-phase material while the actual material contains two phases (filaments and the matrix). Hence, delamination in the present analysis appears as a region of removed elements rather than a region where de-bonding between adjoining phases has taken place. Despite these differences, the extent of delamination predicted by the current model appears comparable to that observed experimentally. Also, the extents of back-face bulging observed experimentally, Fig. 7(a), and the one predicted computationally, Fig. 7(b) are in reasonably good agreement. It should be noted that in the case of the computational analysis some of the elements at the armor-panel back-face in which filament failure has taken place attained a very low level of stiffness which made them undergo relatively large strains. This is the main cause of the observed "bumps" at the armor-panel back-face.

(c) In the case of a 22-mm thick armor panel impacted by a non-armor-piercing M193 projectile at an initial velocity of 800 m/s, both the experiment, and the numerical results show only a partial penetration of the armor with comparable depth of the penetration holes, Fig. 8(a) and (b). As in the case of Fig. 7(a) and (b), the present computational analysis predicts reasonably well the extent of delamination within the armor and the extent of back-face bulging. Again, low stiffness elements containing failed filaments are the main cause of the observed bumps at the armor-panel back-face, Fig. 8(b).

In his work, Iremonger [33] identified three distinct regions of armor failure when subjected to armor-piercing and non-armor-piercing small caliber projectiles: (a) an initial armor-penetration phase dominated by fiber shearing/cutting by the projectile and to a larger extent by plastic deformation of the projectile: (b) extensive delamination of the composite material accompanied by destabilization and break-up/fragmentation of the projectile; and (c) extensive stretching/bulging of the armor back-face which was accompanied by extensive stretching of the fibers enabling armor to absorb substantial portion of the projectile's kinetic energy. The computational results obtained in the present work (e.g. Fig. 7(b)) clearly confirmed the existence of these three stages of projectile/armor interaction suggesting that the proposed material model for 0°/90° cross-plied UHMWPE-based armor-grade composite is physically sound.

4.3. Temporal evolution of the back-face bulge

In Ref. [33], the temporal evolution of the armor back-face bulge height and diameter was reported for only one armor/bullet/testing condition. This condition corresponds to a 32-mm thick armor test panel, M855 bullet and the initial bullet velocity of 900 m/s. The results obtained in Ref. [33] for the bulge height and for the bulge diameter are displayed in Fig. 9(a) and (b), respectively, and they are denoted using filled square symbols. The corresponding computational results obtained in the present work are also displayed in these figures and they are denoted using filled circular symbols. A simple examination of the results displayed in Fig. 9(a) and (b) reveals that: (a) while the initial rate of increase of the back-face bulge height predicted by the present analysis is comparable to that measured experimentally, Fig. 9(a), the computational results under predict the bulge height by ~5–10 mm. There are several potential reasons for this disagreement, the main one being: (i) both the initial projectile velocity and the bulge-height measurements utilized in the work of Iremonger [33] were associated with experimental errors as high as ±5%; and (ii) the extents of projectile damage/fragmentation were likely different in the experiment and in the computational analysis. Unfortunately, no detail information was reported by Iremonger [33] regarding the extent of projectile damage/fragmentation. In other words, the observed experiment/computation discrepancy cannot be solely interpreted as a deficiency of the present model. The computed temporal evolution of the bulge height displayed in Fig. 9(a) shows a decrease in the bulge height after approximately 160 μs. This decrease is associated with the elastic relaxation of the armor-panel back-face after the projectile was defeated and pushed back. Similar observation was not made by Iremonger [33]. Instead, the bulge height has continued to increase, Fig. 9(a). The reason for this discrepancy is that in the work of Iremonger [33] the projectile was typically left buried within the partially penetrated armor panel preventing back-face elastic relaxation; and (b) except for the very initial stage of armor penetration by the projectile, the experimentally measured and computationally predicted temporal evolutions of the back-face bulge diameter are in reasonably good agreement, Fig. 9(b).

4.4. A brief discussion

As stated earlier, the main objective of the present work was to develop, parameterize and validate, (against the relevant experimental results), a simple physically based computationally efficient material model for a prototypical 0°/90° cross-plied oriented polyethylene fiber-based armor-grade composite material. The relevant experimental results were taken from the work of Iremonger [33]. The material-model validation was carried out by constructing a transient non-linear dynamics finite-element model consistent with the experimental setup used in the work

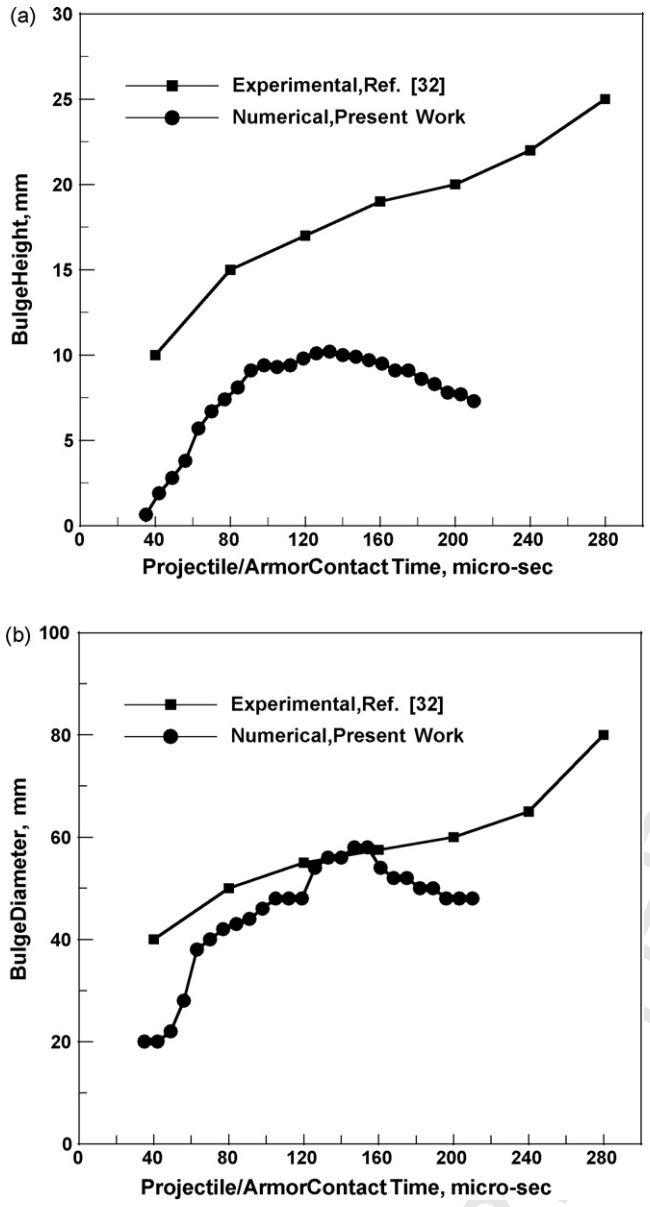

Fig. 9. A comparison between the experimental results obtained in Ref. [33] and their computational counterparts obtained in the present work pertaining to the temporal evolution of: (a) the height and (b) the diameter of a delamination-induced bulge at the armor back-face for the case of a M855 bullet initially propelled at a velocity of 900 m/s impacting a 32-mm thick test panel.

of Iremonger [33]. The key experimental results obtained in Ref. [33] were then compared with their computational counterparts obtained in the present work to judge the validity of the present model. The obtained level of qualitative and quantitative agreement between the two sets of results suggests that the proposed material model is capable of capturing the essential behavior of a prototypical 0°/90° cross-plied UHMWPE-based armor-grade composite material. While the present work was focusing on the initial development, parameterization and validation of the material model, in our future work, the model will be used to investigate in greater details the competition and interplay between various deformation, fracture and energy-dissipation phenomena which control armors ability to defeat projectiles by absorbing their kinetic energy.

5. Summary and conclusions

Based on the work presented and discussed in the present manuscript, the following main summary remarks and conclusions can be drawn:

1. A simple unit-cell continuum-damage-based material model for prototypical cross-plied unidirectional UHMWPE filament-based armor-grade composites has been developed and parameterized.
2. To validate the model, a series of transient non-linear dynamics finite-element computations pertaining to the impact of either an armor-piercing or a non-AP 5.56-mm caliber full-metal jacketed bullet into a 11–32-mm thick armor test panel were carried out and the results obtained were compared with their experimental counterparts reported in Ref. [33].
3. This comparison suggested that, for the most part, the proposed model realistically accounts for the observed behavior of the cross-plied unidirectional UHMWPE filament-based armor-grade composites under the specified ballistic loading conditions. The good computation/experiment agreement pertains to the success of the armor panels of different areal densities in defeating the bullets at different initial bullet velocities, post-mortem spatial distribution of damage within the panel and the temporal evolution of a bulge at the back-face of the armor.
4. The computational analysis was also able to clearly delineate three different stages of armor penetration by the projectile: (a) initial filament shearing/cutting dominated stage; (b) an intermediate stage characterized by pronounced filament/matrix de-bonding/decohesion; and (c) the final stage associated with the extensive bulging of the armor-panel back-face within which pronounced filament stretching leads to major absorption of the projectile kinetic energy.

Uncited reference

[1].

Acknowledgements

The material presented in this paper is based on work supported by the U.S. Army/Clemson University Cooperative Agreements W911NF-04-2-0024 and W911NF-06-2-0042.

References

[1] ANSYS/Autodyn version 11.0, User Documentation, Century Dynamics Inc., a subsidiary of ANSYS Inc., 2007.
[2] ABAQUS version 6.7, User Documentation, Dessault Systems, 2007.
[3] B.L. Lee, J.W. Song, J.E. Ward, J. Compos. Mater. 28 (13) (1994) 1202–1226.
[4] B.L. Lee, T.F. Walsh, S.T. Won, H.M. Patts, J.W. Song, A.H. Mayer, J. Compos. Mater. 35 (2001) 1605–1635.
[5] D.C. Prevorsek, Y.D. Kwon, H.B. Chin, Polym. Eng. Sci. 34 (1994) 141–152.
[6] G. Zhu, W. Goldsmith, C.K.H. Dharan, Int. J. Solids Struct. 29 (4) (1992) 399–420.
[7] G. Zhu, W. Goldsmith, C.K.H. Dharan, Int. J. Solids Struct. 29 (4) (1992) 421–424.
[8] T.L. Schuman, Proceedings of the 24th SAMPE International Technical Conference, 1992, pp. 280–290.
[9] C.L. Segal, Proceedings of the 23rd SAMPE International Technical Conference, 1991, pp. 651–660.
[10] P.G. Riewald, F.H.H. FolgarYang, W.F. Shaughnessy, Proceedings of the 23rd SAMPE International Technical Conference, 1991, pp. 684–695.
[11] T.S. Thomas, Proceedings of the 22nd SAMPE International Technical Conference, 1990, pp. 304–318.
[12] D.C. Prevorsek, H.B. Chin, Development of a Light Weight Spectra Helmet, Phase I Interim Technical Report from AlliedSignal Inc. to U.S. Army Natick RD&E Center, Natick, MA, DAAK60-87-C-0089/D, 1988.
[13] J.W. Song, G.T. Egglestone, Proceedings of the 19th SAMPE International Technical Conference, 1987, pp. 108–119.

[14] J.G. Donovan, B. Kirkwood, F. Figucia, Development of Lower Cost Ballistic Protection, U.S. Army Natick RD&E Center, Natick, MA, Technical Report Natick/TR-85/019L, 1985.
[15] L.C. Lin, A. Bhatnagar, H.W. Chang, Proceedings of the 22nd SAMPE International Technical Conference, 1990, pp. 1–13.
[16] J.C. Smith, J.M. Blandford, H.F. Schiefer, Text Res. J. 30 (10) (1960) 752.
[17] J.C. Smith, J.M. Blandford, K.M. Towne, Text Res. J. 32 (1) (1962) 67.
[18] D. Roylance, A. Wilde, G. Tocci, Text Res. J. 43 (1973) 34–41.
[19] P.M. Cunniff, Text Res. J. 62 (9) (1992) 495–509.
[20] R.W. Dent, J.G. Donovan, Projectile Impact with Flexible Armor—An Improved Model, U.S. Army Natick RD&E Center, Natick, MA, Technical Report Natick/TR-86/044L, 1986.
[21] C.Y. Hsieh, A. Mount, B.Z. Jang, R.H. Zee, Proceedings of the 22nd SAMPE International Technical Conference, 1990, pp. 14–27.
[22] N. Critescu, L.E. Malvern, R.L. Sierakowski, Failure Mechanisms in Composite Plates Impacted by Blunt-Ended Penetrators, Foreign Object Impact Damage to Composites, ASTM, Philadelphia, PA, ASTM STP #568, 1975, pp. 159–172.
[23] D.S. Cairs, P.A. Lagace, AIAA J. 27 (11) (1989) 1590–1596.
[24] R. Frissen, T. Peijs, A. Verlinde, Proceedings of 16th International Symposium on Ballistics, San Francisco, September 1996.
[25] P.M. Cunniff, Proceedings of 18th International Symposium on Ballistics, San Antonio, November 1999, p. 1303.
[26] R. Clegg, C. Hayhurst, J. Leahy, M. Deutekom, Proceedings 18th International Symposium on Ballistics, San Antonio, November 1999, p. 791.
[27] A.M. Floyd, K. Williams, R. Varziri, K. Kanji, A. Pourtasip, Proceedings of 18th International Symposium on Ballistics, San Antonio, November 1999, p. 877.
[28] P.M. Cunniff, J. Ting, Proceedings of 18th International Symposium on Ballistics, San Antonio, November 1999, p. 822.
[29] G.R. Johnson, R. Beissel, P.M. Cunniff, Proceedings of 18th International Symposium on Ballistics, San Antonio, November 1999, p. 862.
[30] X. Guan, N. Birnbaum, Proceedings of 18th International Symposium on Ballistics, San Antonio, November 1999, p. 1107.
[31] M.J.N. Jacobs, J.L.J. Van Dingenen, J. Mater. Sci. 36 (2001) 3137–3142.
[32] M.J.N. Jacobs, J.H.M. Beugels, M. Blaauw, Process for the Manufacture of a Ballistic-Resistant Moulded Article, US Patent 7,288,314 B2 (October 2007).
[33] M.J. Iremonger, International Symposium on Ballistics, San Antonio, November 1999, pp. 946–953.
[34] M. Grujicic, B. Pandurangan, U. Zecevic, K.L. Koudela, B.A. Cheeseman, Multidiscip. Model. Mater. Struct. 3 (2007) 287–312.
[35] B.A. Cheeseman, T.A. Bogetti, Compos. Struct. 61 (2003) 161–173.
[36] M. Grujicic, Y.P. Sun, K.L. Koudela, Appl. Surf. Sci. 253 (2007) 3009.

Please cite this article in press as: M. Grujicic, et al., Mater. Sci. Eng. A (2008), doi:10.1016/j.msea.2008.07.056